

A test of the advection-condensation model for subtropical water vapor using stable isotopologue observations from Mauna Loa Observatory, Hawaii

John V. Hurley,^{1,2} Joseph Galewsky,¹ John Worden,³ and David Noone^{4,5}

Received 3 May 2012; revised 6 September 2012; accepted 7 September 2012; published 13 October 2012.

[1] Subtropical humidity plays a critical role in the radiative balance of the planet, and there is a need for adequate description of the controls on water vapor distributions. This study tests whether an advection-condensation model, combined with Rayleigh distillation, can describe observed humidity and water vapor isotope ratios of the subtropical free troposphere. A field campaign, from 9 October to 6 November, 2008, included continuous in situ measurement of water vapor stable isotope ratios at the NOAA Mauna Loa Observatory (MLO), Hawaii. Last saturation patterns for air at the MLO were determined using both Lagrangian back-trajectory and Eulerian model techniques. Last saturation occurs primarily along midlatitude storm tracks (~65%), and secondarily near Hawaii (~10%) within mesoscale convective systems. Periods of lower δD values at MLO correspond to extra-tropical last saturation, while elevated δD corresponds with saturation locations near Hawaii. To a first order, the conditions of last saturation are found to set not only the humidity but also the water vapor isotope ratio. In the absence of mixing, reconstructed q and δD values underestimate the observations. Experimental reconstructions demonstrate that variable amounts of mixing within the free troposphere and about 2% vapor influx mixing per hour from the boundary layer can explain the observed q and δD values. A last saturation model provides a reasonable description of humidity and water vapor isotope ratios of the subtropical free troposphere and results are sensitive to the treatment of mixing of air parcels last saturated in distinctly different regions of the atmosphere.

Citation: Hurley, J. V., J. Galewsky, J. Worden, and D. Noone (2012), A test of the advection-condensation model for subtropical water vapor using stable isotopologue observations from Mauna Loa Observatory, Hawaii, *J. Geophys. Res.*, 117, D19118, doi:10.1029/2012JD018029.

1. Introduction

[2] Stable isotopes of hydrogen and oxygen are tracers of the atmospheric hydrologic cycle [Gat, 1996], and the importance of subtropical humidity to Earth's radiative balance is well documented [Hansen *et al.*, 2005]. The present study of subtropical humidity uses stable isotopes in the context of a last saturation framework. The humidity of the

subtropical middle troposphere is, to a first order, a function of the conditions at which the air was last saturated [Held and Soden, 2000; Pierrehumbert *et al.*, 2007]. The humidity of the subtropical free troposphere has been quantitatively described in last saturation frameworks using both Lagrangian and Eulerian reference frames [Cau *et al.*, 2007; Dessler and Minschwaner, 2007; Galewsky *et al.*, 2005; Sherwood, 1996]. Although the advection-condensation is capable of explaining first order details of humidity as products of the large-scale circulation and temperature fields [Pierrehumbert and Roca, 1998], it is limited in ability to fully account for cloud processes and regional heterogeneity in the water vapor field [Berkelhammer *et al.*, 2012; Emanuel and Pierrehumbert, 1996; Risi *et al.*, 2012a, 2012b; Sun and Lindzen, 1993; Wright *et al.*, 2009].

[3] Like humidity, the isotopic composition of water vapor in the dry subtropics depends not only on last saturation conditions, but also on the degree to which parcels are mixed from different regions of the atmosphere. By measuring and studying water vapor stable isotope compositions in the subtropical middle troposphere, aspects of the processes that influence the humidity of this region can be constrained in

¹Department of Earth and Planetary Sciences, University of New Mexico, Albuquerque, New Mexico, USA.

²Now at Department of Geology and Geophysics, Yale University, New Haven, Connecticut, USA.

³Jet Propulsion Laboratory, California Institute of Technology, Pasadena, California, USA.

⁴Department of Atmospheric and Oceanic Sciences, University of Colorado Boulder, Boulder, Colorado, USA.

⁵Cooperative Institute for Research in Environmental Sciences, University of Colorado Boulder, Boulder, Colorado, USA.

Corresponding author: J. V. Hurley, Department of Geology and Geophysics, Yale University, New Haven, CT 06520, USA. (john.hurley@yale.edu)

ways that are not possible by measuring humidity alone [Noone, 2012]. Specifically, the isotopic composition differentiates vapor that has been exposed to mixing from vapor from a pure distillation process, and in so doing, can provide a test of the advection-condensation paradigm. A conceptual view of the isotopic composition being described as a combination of distillation combined with atmospheric mixing has been confirmed by GCM studies of the zonal mean [Noone, 2008] and in three dimensional idealized [Galewsky and Hurley, 2010] experiments, yet it remains to be confirmed with observations. Noone *et al.* [2011] showed for the case of Mauna Loa that the isotopic composition of dry nighttime air is crudely consistent with a Rayleigh process when the dew point temperature is significantly below freezing. However, the neglect of either the condensation history prior to ice formation and the influence of kinetic effects during ice deposition places limits on the accuracy of a simple Rayleigh assumption [Cuffey and Vimeux, 2001; Jouzel *et al.*, 1987]. Nonetheless, the use of a simple temperature constraint on a Rayleigh model provides a conceptually satisfying extension of the traditional advection-condensation models that relate the specific humidity (q) of sub-saturated air to condensation history; colder last saturation corresponds with drier air and vice versa. Given this expected relationship, measurements of isotopic composition of water vapor holds significant potential to provide additional quantitative information with which to evaluate the “last saturation” description of the humidity distribution in the subtropics [Galewsky and Hurley, 2010; Noone *et al.*, 2011].

[4] In the last decade, Earth observing satellites have achieved the capability to measure a vertically integrated water vapor isotope ratio [Brown *et al.*, 2008; Payne *et al.*, 2007; Worden *et al.*, 2007], but due to the nature of such satellite observations, spatial and temporal resolutions are relatively coarse, and accuracy is limited. Sayres *et al.* [2010] demonstrated the usefulness of airborne measurement of water vapor isotopic composition for understanding the mechanisms that influence humidity of the tropical tropopause layer. Table-top laser-based instruments are also becoming more readily available, allowing for in situ continuous measurement of water vapor stable isotope composition [Gupta *et al.*, 2009; Iannone *et al.*, 2010; Lis *et al.*, 2008]. This measurement approach is more efficient, less labor intensive, than sample collection with either a flask or cryogenic trap and subsequent laboratory analysis with a mass spectrometer [Johnson *et al.*, 2011]. Here, we focus on the results of the laser-based component of a field campaign of stable isotope measurements, which included the continuous in situ laser measurements as well as daily to sub-daily conventional flask and cryogenic trap sampling [Johnson *et al.*, 2011; Noone *et al.*, 2011].

[5] In this study, an Eulerian and a Lagrangian last saturation model, are used to simulate and reconstruct q and water vapor hydrogen isotope ratios. Advection-condensation models are used to characterize a month-long time series of nighttime observations measured from the north Pacific subtropical free troposphere near the summit of Mauna Loa, Hawaii [Noone *et al.*, 2011]. The regions where air parcels observed at Mauna Loa are saturated upstream are identified and the water vapor isotope composition of the subtropical free troposphere is explained in terms of the large-scale

advection-condensation hypothesis. We assess the role of mixing on subtropical humidity and stable isotope composition through experiments where we use the advection-condensation model, and vary the amount of mixing, to reconstruct the observed time series of nighttime isotope ratios. Two varieties of mixing are considered; air mass mixing within the free troposphere and mixing of evaporated source water from the surface.

2. Data and Models

2.1. Observations at MLO

[6] Continuous measurements of water vapor stable isotope compositions were made at the National Oceanic and Atmospheric Administration’s (NOAA) Earth System Research Laboratory at Mauna Loa, Hawaii (Mauna Loa Observatory [MLO]) [Noone *et al.*, 2011]. References to dates and times in this paper are local Hawaiian time, and all references are in units of day of the year (DOY). The field campaign took place from 9 October (DOY 283) to 6 November, 2008 (DOY 311). Water vapor mixing ratio and water vapor hydrogen and oxygen isotope ratios were measured in the ambient air approximately every six seconds with a Picarro Incorporated Isotopic Water Vapor Analyzer (model L1002), using Wavelength Scanned Cavity-Ring-down Spectroscopy (WS-CRDS) [Gupta *et al.*, 2009]. Mixing ratio and isotope compositions were also measured every ten seconds with a Los Gatos Research Incorporated Water Vapor Isotope Analyzer (model 908–0008), using off-axis cavity enhanced spectroscopy. A discussion of the flask and cryogenic trap sampling results is presented in Johnson *et al.* [2011].

[7] The laser-based techniques operate by passing an infrared laser through a continuous stream of air in a pressure and temperature controlled optical cell. On the basis of the absorptivity at specific wavelengths characteristic of the different isotopologues of water, the mole fraction concentration of each isotopologue can be computed. The data are reported in conventional delta notation (δ), where,

$$\delta = \left[\left(R_{\text{sample}} / R_{\text{standard}} \right) - 1 \right] \times 1000, \quad (1)$$

in units of parts per thousand (per mil [‰]). R is the ratio of heavy to light isotope. For hydrogen, the heavy and light isotopes are deuterium (D) and hydrogen (H), and the standardized isotope ratios are expressed as δD values. The standard for both hydrogen and oxygen isotope ratios is the Vienna Standard Mean Ocean Water (VSMOW) with a defined value of 0.0‰. The precision reported for the Picarro and Los Gatos instruments are 1‰ and 0.2‰, for ranges of humidity mostly higher than the typical humidity at MLO [Johnson *et al.*, 2011]. The 6-s precision for the Picarro instrument at between 500 and 10,000 ppmv H_2O , as observed at MLO is about 18‰ (see Noone *et al.* [2011] for further discussion). All isotope measurements made during the campaign were subsequently corrected to the VSMOW scale by Johnson *et al.* [2011]. The corrections were made to account for the laser-based instruments’ bias to underestimate the heavy to light isotope ratio when the water vapor concentration is particularly low. For the purposes of this study, Johnson *et al.*’s [2011] corrected versions of both the Picarro and Los Gatos measurements are nearly

indistinguishable from each other, and for simplicity we use the corrected Picarro δD data, again focusing on nighttime observations. The in situ oxygen isotope data could not be bias-corrected because oxygen isotope ratios could not be measured from the flask samples, therefore we focus on the hydrogen isotope results.

2.2. Lagrangian Advection-Condensation Modeling

[8] For the Lagrangian advection-condensation perspective, 12,000 back-trajectories were calculated using the NOAA Hybrid Single Particle Lagrangian Integrated Trajectory Model (HYSPLIT) [Draxler and Hess, 1997]. Air parcels were tracked in three dimensions along back-trajectories launched from 100 grid points near MLO every six hours over the course of the campaign period. In this way, a suite of 100 back-trajectories was computed for each six-hourly time step. The latitude and longitude range of the trajectory launch positions are 19.5°N to 20.25°N and 156.1°W to 154.85°W, compared with 19.54°N and 155.6°W for the MLO. The altitude range for the launch positions was 3395 to 3415 m (about 640 to 670 hPa), which is comparable to about the altitude of 3400 m and an average pressure level of about 680 hPa for the MLO. The 6-hourly ERA-Interim reanalyses [Dee et al., 2011; Simmons et al., 2007] for September, October, and November 2008 were used for the trajectory simulations. (We also completed a smaller set of back-trajectory calculations using the NCEP-NCAR reanalyses [Kalnay et al., 1996] but found the large-scale advection patterns to be consistent and we focus primarily on the ERA-Interim calculations.) Vertical motions were taken from the reanalysis output. Trajectories were run backward for 10 days, as in Pfahl and Wernli [2008], tracking position, temperature, humidity, precipitation, and relative humidity each hour. We consider air parcels to have been last saturated when they encounter the minimal absolute difference between (i) specific humidity of the parcel, q , at the time of launch, and (ii) saturation specific humidity (q^*) along the back-trajectory. This is similar to the technique of Cau et al. [2007]. We then evaluated relative humidity between last saturation and MLO. If relative humidity was found to increase between last saturation and MLO, then the time and position of maximum relative humidity encountered between that last saturation and MLO was selected as the revised last saturation condition. We found the mean change in q , between last saturation and MLO, to be less than 0.1 g/kg suggesting conservation since last saturation. We use this criterion rather than a simple relative humidity threshold because parcels rarely experience a relative humidity of 90 percent along these Lagrangian back-trajectories and for some parcels, the relative humidity does not exceed 80 percent over a 10-day tracking period. This is not surprising as precipitation arises mainly from the convective scheme, which can be triggered irrespective of the relative humidity at the grid scale. The specific humidity reconstruction from a relative humidity based last saturation threshold (not shown) is a qualitatively poorer approximation of the observed specific humidity, compared with the specific humidity reconstructed presented here. Once the time and position of last saturation is identified, then we set q , at the time of the parcel launch, equal to q^* from the HYSPLIT output, at the time and location of last saturation along the back-trajectory. The isotope composition, at last saturation, is calculated assuming Rayleigh fractionation up from the lifting condensation level (LCL) to the time and

location of last saturation along the back-trajectory. For Rayleigh fractionation throughout this paper, we assume that air exiting at the top of the marine boundary layer has a specific humidity that reflects the meridional distribution of near-surface specific humidity, where specific humidity ranges from about $q = 35$ g/kg in the tropics to about $q = 1-2$ g/kg at the poles, and around 20 g/kg near Hawaii. The hydrogen isotope ratio of the initial vapor is assumed to be $\delta D_{src} = -90\%$ and the air is considered lifted from the surface dry adiabatically to the LCL of about 850 hPa.

[9] The Lagrangian model does not account for mixing of air from various last saturation regions. To explore the role of mixing, we add a contribution of marine boundary layer air to the water vapor derived from the Lagrangian back-trajectory, in a manner similar to the Eulerian model's source tracer (discussed below).

2.3. Eulerian Advection-Condensation Modeling

[10] For the Eulerian modeling, six-hourly NCEP Reanalysis was used to drive an atmospheric tracer transport model configured with a network of zonally symmetric last saturation water vapor tracers, following the methods of Galewsky et al. [2005] and Hurley and Galewsky [2010a]. The diagnostic simulation was conducted using the National Center for Atmospheric Research Model for Atmospheric Transport and Chemistry (MATCH) [Rasch et al., 1997]. The weather for September through November 2008 was simulated and September results are discarded as a model spin-up period. We focus on last saturation probability (LSP [c]) results for the field campaign that ran from early October to early November. The tracer simulation was completed at a T62 horizontal grid and 28 pressure levels in the vertical as dictated by the underlying NCEP wind and temperature fields (see Galewsky et al. [2005] for details).

[11] The model operates such that upon saturation of a grid point, when the relative humidity meets or exceeds 90 percent, the LSP for the tracer domain in which the grid point resides is set to 1 [Galewsky et al., 2005]. The LSP for all other tracer domains, for the grid point, are set to zero, and the advection scheme redistributes LSPs between saturation events. The resultant six-hourly time series of a tracer's concentrations, or LSPs, then represents the time variable probability that air at the MLO was last saturated within the tracer's domain. The tracer domain network was configured over the northern hemisphere, from latitude 10°S to 90°N. All 100 tracer domains were zonally symmetric around the globe and were 10° of latitude wide and 2 vertical pressure levels deep. For each 10° of latitude, there were 10 vertically stacked tracer domains from above the lowest model level up to the tropopause. In addition to the water vapor tracer domain network, which accounts for most of the air at MLO, an extra tracer referred to as the source tracer handles water that is evaporated from the surface, and is transported from the boundary layer to the free troposphere, but that has not yet encountered saturation. In this manner, we can account for water vapor at MLO by two paths, either from air last saturated within the free troposphere, or as water evaporated from the surface but not yet processed through a cloud. Convection in MATCH is parameterized with a deep cumulus scheme [Zhang and McFarlane, 1995] that entrains and detrains laterally but does not remove tracers during condensation in convection [Galewsky et al., 2005].

2.4. Humidity and Isotope Reconstruction Calculations

[12] Water vapor mixing and isotope ratios for the air at the MLO were reconstructed using both the Lagrangian and Eulerian advection-condensation model results. This allows for assessment of the influence that large-scale mixing and circulation have on the temporal variability of water vapor isotope and mixing ratios.

2.4.1. Lagrangian Calculations

[13] First, we reconstruct the time series for the amount of water vapor at MLO, based on saturation conditions from the Lagrangian back-trajectory simulations. For the back-trajectory analysis, q at time t , $q(t)$, is considered equal to the sum of (i) q^* along the back-trajectory at Lagrangian last saturation q^*_{lls} and (ii) an amount of vapor mixed up from the evaporative source of the marine boundary layer (q_{lsrc}). q^*_{lls} is calculated from the temperature and pressure fields taken from the HYSPLIT output. The marine boundary layer vapor ($q_{lsrc} = 20$ g/kg), is assumed to be derived from an ocean of around 20°C, it is then lifted dry adiabatically up to the LCL at 850 hPa, and then moist adiabatically up to MLO at about 700 hPa. Here we assume that 1 percent of the vapor at MLO comes from the marine boundary layer to MLO, per hour since last saturation. By mixing as a function of the time since last saturation we allow for more source vapor mixing for trajectories that are longer in duration. We explore the influence of variable amounts of mixing via a series of sensitivity experiments.

[14] For reconstructing the time series of δD values at the MLO, from the Lagrangian results, we combine HYSPLIT results on last saturation conditions, with δD values calculated for simple Rayleigh fractionation. δD at the MLO $\delta D(t)$ is computed as the mass-weighted combination of the hydrogen isotope ratio modeled at the time and location of last saturation and the hydrogen isotope ratio of the portion of vapor contributed from the marine boundary layer. The method is similar to that used to identify the isotope ratio of water in the region of organized tropical convection associated with the Madden-Julian Oscillation [Berkelhammer et al., 2012]. The Lagrangian reconstruction of heavy to light isotope ratio at MLO R_{MLO} , is solved as

$$R_{MLO}(t) = ((1 - k) \times [(HDO_{lls}] + k \times HDO_{lsrc}) \cdot ((1 - k) \times [H_2O_{lls}] + k \times [H_2O_{lsrc}])^{-1}, \quad (2)$$

where the *lls* and *lsrc* subscripts indicate the Lagrangian last saturation and source water (marine boundary layer vapor), HDO and H₂O are the heavy and light isotopologues, and k is the fraction of water at MLO from the source or marine boundary layer. For the ERA-Interim –based Lagrangian reconstruction HDO_{lls} and H_2O_{lls} from equation (2) represent the sum of HDO and H₂O values from the suite of 100 back-trajectories calculated per each time step. Whereas, for the NCEP –based Lagrangian reconstruction, HDO_{lls} and H_2O_{lls} represent the HDO and H₂O values along a single trajectory.

2.4.2. Eulerian Calculations

[15] For the Eulerian humidity calculation, $q(t)$ is calculated as a sum, across tracer domains i , of the product of the LSP c_i , and the saturation specific humidity at Eulerian last saturation tracer domains $q^*_{i,els}$, by

$$q(t) = (c_{esrc} \times q_{esrc}) + \sum_i (c_i \times q^*_{i,els}) \quad (3)$$

c_{esrc} is the probability of contribution from the source vapor, q_{esrc} refers to the specific humidity of that water vapor evaporated from the marine boundary and not processed through a cloud. For the Eulerian model, the first term on the right-hand side ($c_{esrc} \times q_{esrc}$), is calculated by MATCH per time step as a function of position. This technique for reconstructing q from a LSP distribution for an Eulerian network of last saturation tracer domains follows that of Galewsky et al. [2005, 2007], and Hurley and Galewsky [2010a]. $q^*_{i,els}$ is calculated from the reanalysis temperature and pressure.

[16] For reconstructing the time series of δD values at the MLO, from the Eulerian results, we combine the last saturation distribution results, with a suite of δD values calculated for each tracer domain assuming Rayleigh fractionation from the LCL (850 hPa), up to each tracer domain. As indicated earlier, the Eulerian reconstruction of δD at the MLO implicitly does assume the air to be a product of mixing of air from various last saturation regions. As such, the hydrogen isotope ratio of water vapor at each time step $R_{MLO}(t)$ is calculated following equations (5) and (6) from Galewsky and Hurley [2010], by

$$R_{MLO}(t) = \left([c_{esrc} \times HDO_{esrc}] + \sum_i [c_i \times HDO_{i,els}] \right) \times \left([c_{esrc} \times q_{esrc}] + \sum_i [c_i \times q^*_{i,els}] \right)^{-1}. \quad (4)$$

[17] The *els* and *esrc* subscripts refer to Eulerian last saturation and marine boundary layer evaporative source water. We assume Rayleigh fractionation associated with the density-weighted temperature of last saturation at tracer domain i . As with the Lagrangian reconstruction, the initial marine boundary layer vapor undergoes Rayleigh fractionation up to the temperature and pressure of last saturation.

[18] To summarize our approach, we use both HYSPLIT Lagrangian back-trajectories, and we use MATCH, with an Eulerian water vapor tracer configuration, to identify last saturation conditions for air at MLO. From both methods, we are able to compute the water vapor mixing and stable isotope ratios at MLO, compare them to observations, and understand the processes that set these values. Differences between the Eulerian and Lagrangian results can be considered to reflect different treatments of advection, mixing, or physical parameterization, such as representation of cloud processes. We used the NCEP Reanalysis for the Eulerian simulation and both the ERA-Interim Reanalysis and the NCEP Reanalysis for the Lagrangian back-trajectory calculations. Advection, or the large-scale flow does not significantly vary over the Pacific during the measurement period between the ERA-Interim and the NCEP Reanalysis (not shown) (NOAA, Reanalysis Intercomparison and Observations, 2011, <http://reanalyses.org/atmosphere/pages?order=title&sort=desc>). Different representations of mixing account for differences between our Eulerian and Lagrangian results. The Eulerian based analysis explicitly mixes air from various last saturation regions as well as from a source tracer that handles water evaporated from the surface. The Lagrangian analysis based on the ERA-Interim Reanalysis mixes air from a suite of back-trajectories per time step, while our Lagrangian analysis based on the NCEP Reanalysis does not include air mass

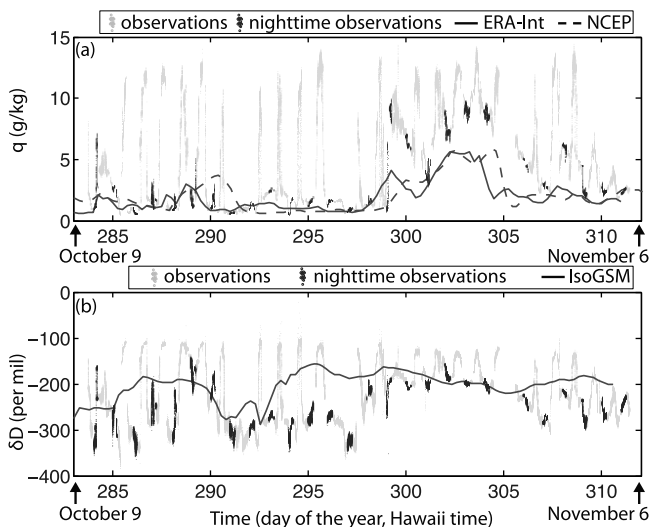


Figure 1. (a) Water vapor mixing ratio; gray - in situ continuous measurements made at MLO with Picarro instrument (corrected for bias by Johnson *et al.* [2011]), overnight values in black, Reanalysis output for reference (solid - ERA-Interim, dashed - NCEP). (b) Water vapor δD values; gray and black symbols are in situ measurements with color scheme as in Figure 1a, solid line - IsoGSM output for a model grid point near MLO.

mixing within the free troposphere and considers air to have come from a single trajectory. Furthermore, for the ERA-Interim-based analysis, we consider the influence of a source-like tracer. Misrepresentation or absence of representation of cloud processes influences both the Eulerian and Lagrangian reconstructions and likely limits the ability to accurately account for the details of the observations.

3. Results

3.1. Water Vapor Isotope Compositions

[19] Time series for the MLO field campaign water vapor mixing ratios and δD values are shown in Figure 1 and are examined in detail elsewhere [Johnson *et al.*, 2011; Noone *et al.*, 2011; Worden *et al.*, 2010]. The temporal patterns of both water vapor mixing and isotope ratios are similar. The patterns are characterized by diurnal cycles overprinted upon longer period, temporal variability on the order of 2 to 7 days. The diurnal cycle captures the daytime lifting of the top of the boundary layer, the trade wind inversion, and relatively humid air with high δD values. During periods when the overnight conditions at MLO are dry and δD values are low, then the daily range of δD values is from -350‰ to -100‰ . During periods when the nighttime q is relatively higher at MLO and the nighttime water vapor δD values are also relatively higher, then the daily range in δD values at MLO is smaller, about -200‰ to -120‰ . The higher daytime isotope ratios, on the order of -150‰ to -80‰ , are representative of the marine boundary layer and water vapor recently evaporated from the ocean surface [Galewsky *et al.*, 2007; Sharp, 2006]. This has been determined in the case of the MLO time series using a mixing line analysis [Noone *et al.*, 2011]. Diurnal cycles in the height of the trade wind

inversion are primarily related to radiative heating of cloud tops [Brill and Albrecht, 1982] and at Hawaii, the diurnal cycles are related to differential topographic heating.

[20] At night, the boundary layer and the trade wind inversion at Hawaii relax to the typical oceanic boundary layer conditions [Cao *et al.*, 2007], and the air at the sampling site is more representative of the middle troposphere. The air is drier and the water vapor has low δD values. In this paper we focus on the temporal variability, on the order of about 2 to 7 days, of the nighttime humidity and isotope composition. Two pronounced several-day periods define the time series. The first of these is a dry period from about days 290 to 294 with low δD values from about -400‰ to -300‰ . During the later period, about days 300 through 305, the water vapor mixing ratio at MLO is higher, and δD values are higher, around -200‰ . The former is associated with approximately isentropic dry air advection from the north-northeast, while the latter is associated with moist convection near Hawaii [Noone *et al.*, 2011]. Contrasting these two distinctly different hydrologic regimes present a useful quantitative test of the last saturation approach.

[21] Included in Figure 1 (solid lines) for comparison to the observations are model output results for both q from the NCEP Reanalysis and δD values from IsoGSM for a model grid point nearest MLO, from the 700 hPa pressure level. IsoGSM is an isotope enabled GCM that is nudged by NCEP Reanalysis data and output is available for vapor and precipitation [Yoshimura *et al.*, 2008]. The time series of q from the IsoGSM output (not shown), for a grid point near MLO, matches the NCEP data. Time series of q from the Reanalysis match the observed longer period variability of humidity at MLO, but the Reanalysis underestimates the observed humidity during moist events, for instance from days 300 to 305. The Reanalysis does not spatially resolve the topographic feature of Hawaii and so even if the boundary layer processes were well constrained in the vicinity of Hawaii, it is not surprising that the observed diurnal cycle is not reflected in the models. The underestimate of q during the particularly moist event at days 300 to 305 is an example of the limitations of moisture fields in the Reanalysis. This likely reflects an inability of the models to either resolve large-scale advection or represent convective processes that would transport moisture from the boundary layer to MLO. There are recognized biases in the NCEP Reanalysis q , as radiosonde measurements are the only observations assimilated into the q field [Dessler and Davis, 2010]. Time series of the IsoGSM model output δD values do not match the observations particularly well. The Pearson correlation coefficient (r) was calculated from vectors of common length interpolated from the time series of both the nighttime observations and IsoGSM output. The correlation (r), between observed and IsoGSM δD values, is 0.24. Differences between the observations made at MLO and the six-hourly model output highlight the difference between model results and in situ observations. Also, it is likely that the correct set of cloud processes is not represented in IsoGSM, and the moisture transport may be too dispersive [Risi *et al.*, 2010, 2012a]. Moistening of the middle troposphere from mid-level clouds is commonly under-represented in single-column and general circulation models [Chepfer *et al.*, 2008; Woolnough *et al.*, 2010; Zhang *et al.*, 2010].

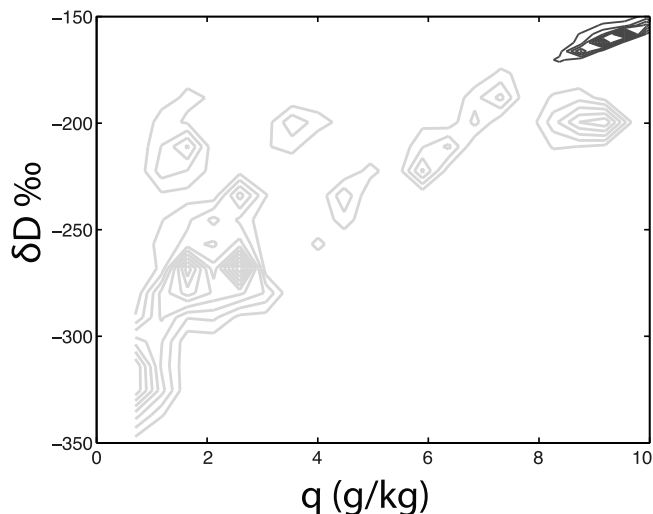


Figure 2. Joint normalized probability distributions of q and δD ; observed over-night distribution (gray contours) and the distribution predicted by a marine boundary layer vapor having undergone Rayleigh fractionation up to the time-variable temperature at MLO (black contours). Contour intervals are 10%.

[22] The distributions of these observations do not follow a simple Rayleigh distribution. This result agrees with an earlier study based on vertical profiles of isotope ratios near MLO by *Galewsky et al.* [2007]. If we assume the water

vapor isotope ratio at MLO to be a function of moist adiabatic lifting of a marine boundary layer vapor ($q = 20 \text{ g/kg}$ and $\delta D = -90\text{‰}$) and Rayleigh fractionation up to the time-variable temperature and pressure of the MLO (Figure 2), the reconstructed δD values are too high by 100‰ to 200‰, underestimate the range of observed δD values, and overestimate the humidity. This joint distribution of Rayleigh fractionation-based δD and q values lie below a mixing line connecting the subtropical marine boundary layer and the extra-tropical upper troposphere. The discrepancy between the observations and a simple Rayleigh fractionation-based prediction further motivates our investigation to understand the processes that determine the distribution of q and δD values in the subtropical middle troposphere.

3.2. Lagrangian Back-Trajectories

[23] The horizontal distribution of last saturation along back-trajectories (Figure 3) indicates that transport of dry air to the MLO follows an anticyclonic pattern after saturation. For readability, a representative subset of 120 trajectories is shown in Figure 3, one for every 100 trajectories. The mean time since last saturation is about 4.5 to 5 days. Most estimated last saturation positions occur over the extra-tropical north Pacific, regardless of the criteria for last saturation threshold. This pattern of transport along an anticyclone trajectory following saturation on the perimeter of the storm-track associates the air at MLO to the midlatitude baroclinic systems that migrate across the Pacific. These two regions, the dry subtropical middle troposphere and the extra-tropical storm track regions, are linked approximately by time-mean

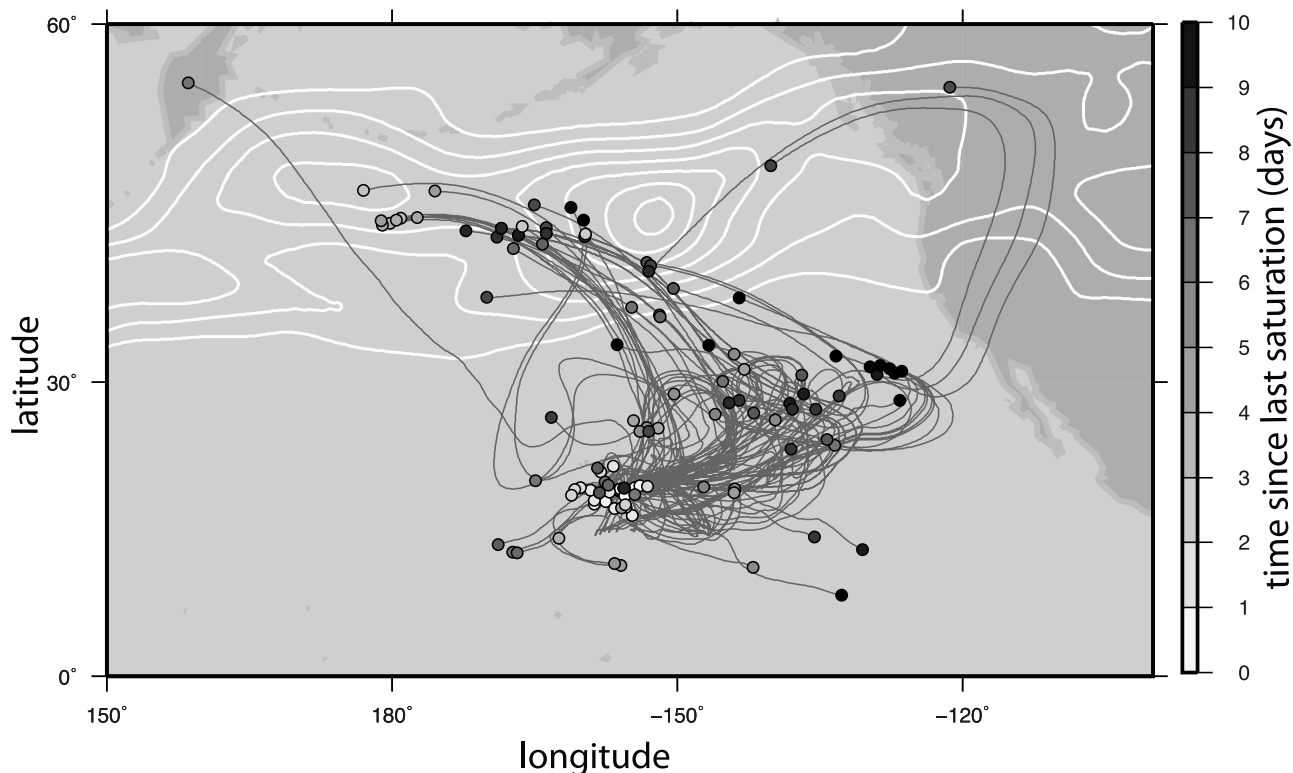


Figure 3. Lagrangian back-trajectories (solid gray lines) that terminate at last saturation (filled circles), using ERA-Interim reanalysis. Contours are eddy kinetic energy (EKE) at 313 hPa, in units of $\text{m}^2 \text{s}^{-2}$. First contour is $250 \text{ m}^2 \text{s}^{-2}$ and contour interval is $50 \text{ m}^2 \text{s}^{-2}$. EKE was calculated for September–October–November 2008. Gray-shading of the filled circles denotes the time, in days, since last saturation.

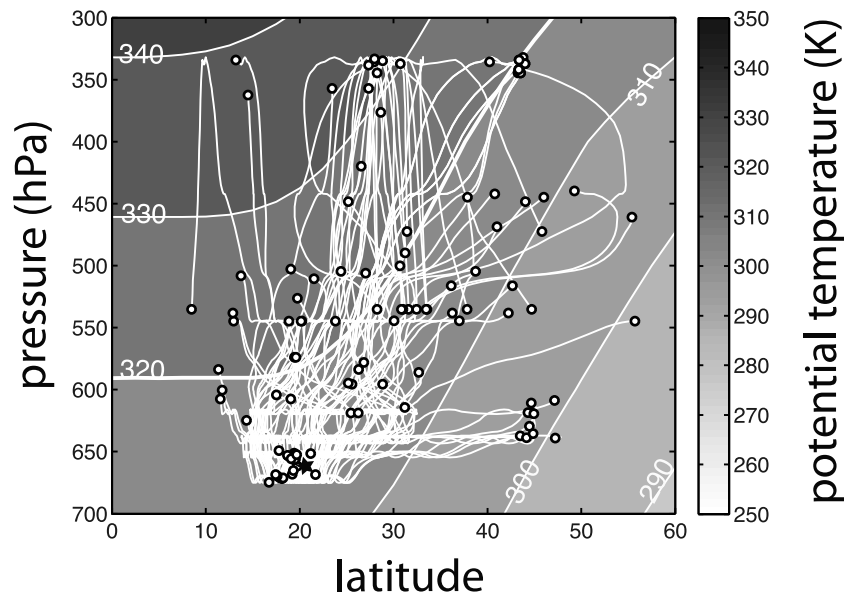


Figure 4. Lagrangian back-trajectories (solid white lines) that terminate at last saturation (black circles), using ERA-Interim reanalysis. Contours are zonal mean potential temperature (time mean for October–November 2008), in units of degrees Kelvin with a 10-degree contour interval. Position of MLO is shown by black star.

surfaces of constant potential temperature, upon which baroclinic eddies dehydrate air and transport it from their moist adiabatic poleward leg to the subtropics. In addition to mid-latitude storms, there is also a large cluster of last saturation locations in the vicinity, east and south, of the Hawaiian Islands. The vertical distribution of last saturation along back-trajectories (Figure 4) shows that these near-Hawaiian last saturation positions are also at an altitude near the MLO, suggesting last saturation associated with mesoscale convective systems. We further distinguish the last saturation regimes using the NCEP Reanalysis model precipitation rate fields (not shown). Eighty to ninety percent of the precipitation total at the latitude of Hawaii across the Pacific is in the form of model convective precipitation. North of about 40°N, the Reanalysis convective precipitation accounts for less than 30% of the model precipitation rate.

[24] Low δD values during the relatively dry interval from about days 290 to 294 correspond to trajectories that encounter last saturation over the northeastern Pacific and northwestern North America (Figure 5a). Last saturation during this interval is associated with a westerly low-pressure storm system that extends from the tropical central Pacific to the northeast across the extra-tropical north Pacific. In contrast, high δD values during the relatively humid interval at MLO from about days 300 to 305 correspond to trajectories that encounter last saturation near Hawaii, within a mesoscale convective system (Figure 5b). These back trajectories are in qualitative agreement with the suite of back-trajectories shown in *Noone et al.*'s [2011] Figure 10.

[25] The distribution of last saturation days (Figure 6) from the Lagrangian analysis shows saturation is primarily associated with a couple of events centered around day 286 and 302 (12 October and 28 October). Infrared satellite images for these two saturation events are shown in the

backgrounds of Figures 5a and 5b. Saturation associated with about day 286 typically occurs between 2 to 6 days along back-trajectories, whereas saturation associated with about day 302 occurs early along back-trajectories, within one or two days. Saturation around day 286 occurs in the midlatitude storm activity over the northeast Pacific, while saturation around day 302 occurs in near-Hawaiian mesoscale convective activity.

3.3. Eulerian Last Saturation Probabilities

[26] The Eulerian modeling approach shows that about 97 percent of the air at the MLO was last saturated within the free troposphere during the field campaign, and the 3 percent remainder of air was from surface evaporation, in broad agreement with the nighttime source estimates derived from an isotope mixing model given by *Noone et al.* [2011]. Figure 7a shows the time-mean LSP distribution for reference air at the MLO. Color shading represents the likelihood that air at the reference position was last saturated within the tracer domain. The sum of LSPs for tracer domains north of 20°N and above 500 hPa indicates that about 65 percent of the air at MLO was last saturated in the extra-tropical upper troposphere, and about 10 percent of the air at MLO is last saturated in the direct vicinity of Hawaii, between 10°N to 30°N and about 750 hPa up to 500 hPa.

[27] To identify last saturation regions associated with the largest magnitude of temporal variability, the standard deviation was calculated from the time series of LSP, for each tracer domain. The standard deviation of LSP is greatest in both the extra-tropical upper troposphere and near Hawaii in the lower-middle troposphere (Figure 7b). Figure 8 shows time series of LSP for those tracer domains with both the greater time-mean LSPs and the greatest temporal standard deviations. Periods of high over-night δD values at the MLO

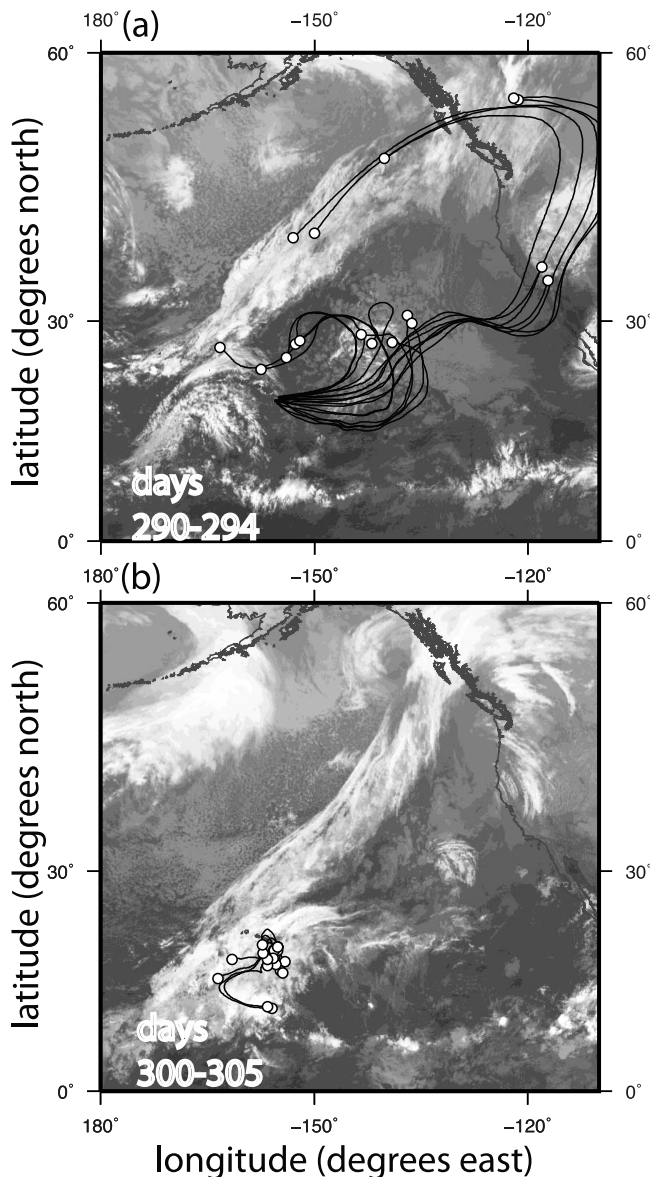


Figure 5. Lagrangian back-trajectories (solid lines, using ERA-Interim reanalysis) plotted over Geostationary Operational Environmental Satellite (GOES) –11 infrared images for a time-slice approximate to the time of last saturation, (a) day 286 and (b) day 302. Trajectories terminate at location of last saturation (filled black circles). Back-trajectories plotted are those for the intervals from days 290 to 294 (Figure 5a), and days 300 to 305 (Figure 5b).

(days 300 to 305) correspond with greater LSP associated with near-Hawaiian tracer domains. During periods of low over-night δD values at the MLO (days 290 to 294), there is greater LSP associated with the extra-tropical upper troposphere. These patterns of LSP are also evident in the time – and Pacific - zonal mean distributions of LSP for discrete time intervals (Figure 9). From days 290 to 294, there is enhanced LSP associated with the extra-tropical upper troposphere (Figure 9a), consistent with Lagrangian back-trajectories that encounter last saturation in the extra-tropical upper troposphere. From days 300 to 305, there is enhanced

near-Hawaiian LSP (Figure 9b), also consistent with the Lagrangian back-trajectories that encounter last saturation near-Hawaii. Mixing of air last saturated in distinctly different regions is prevalent during this latter period when humidity at MLO is relatively high and the air is a mixture of not only parcels last saturated in the extra-tropical upper troposphere, but also of parcels last saturated nearby in the warmer and moister tropical lower troposphere, where water vapor δD values are higher than they are in the extra-tropical upper troposphere.

3.4. Humidity and Isotope Reconstructions

[28] Time series reconstructions of q are presented in Figures 10b and 10c. Included in Figure 10c are both the NCEP and ERA-Interim reanalysis-based Lagrangian reconstructions for specific humidity. Time series curves for plus or minus one standard deviation are included for the ERA-Interim –based Lagrangian reconstruction (Figure 10c). The Lagrangian reconstructions (Figure 10c) show much more variability than the Eulerian reconstruction. Both reconstructions do capture such first order variability as the consistently dry period from about days 290 to 294 and the higher humidity period from days 300 to 305. The Eulerian reconstruction (based on the NCEP Reanalysis) underestimates humidity when the humidity at MLO is high, but captures the first order patterns of temporal variability. This dry bias during the particularly moist event may reflect the shortcomings in the Reanalysis humidity field that were discussed earlier (under-representation of moistening by mid-level clouds). However, the improved Lagrangian reconstruction with the higher-resolution ERA-Interim reanalysis, compared with the NCEP-based reconstruction (Figure 10c), points to a bias related to the resolution of the wind field. The resolution of horizontal wind information limits predictions of small spatial and temporal scale information on the humidity. Note that the q and temperature used in the reconstructions are also from the ERA-Interim and the temporal resolution of the back-trajectory analysis conducted with ERA-Interim is greater than the temporal resolution of the analysis with the NCEP Reanalyses. The mean of the Lagrangian reconstructed values for q compare well with the mean of the overnight observations (midnight to 0600 h); 4.1 g/kg Lagrangian reconstructed, versus 3.32 g/kg observed. Midnight to 0600 h local time is well within the range identified by NOAA as when baseline conditions prevail at MLO for the purpose of sampling background/tropospheric carbon dioxide [Tans and Thoning, 2008]. The mean of q from both the NCEP Reanalysis and the Eulerian reconstruction (also based on the NCEP Reanalysis) underestimate the observed mean; 2.10 g/kg Reanalysis and 2.05 Eulerian reconstructed. Despite underestimating the range of values for q at MLO, the Reanalysis and the Eulerian based reconstructions have higher correlation coefficients to the time series of overnight observations, than does the Lagrangian reconstruction. Correlation coefficients (r) for observed q , compared with q from both the ERA-Interim and NCEP Reanalysis, and the Eulerian and Lagrangian –based reconstructions are; $r = 0.78$ (ERA-Interim), $r = 0.64$ (NCEP), $r = 0.60$ (Eulerian), and $r = 0.44$ (Lagrangian). As with the Reanalysis, the Eulerian approach underestimates the humid end of the range of observed q . The under-estimate of high-humidity during convective periods at MLO supports the notion that under-representation of moistening from mid-level

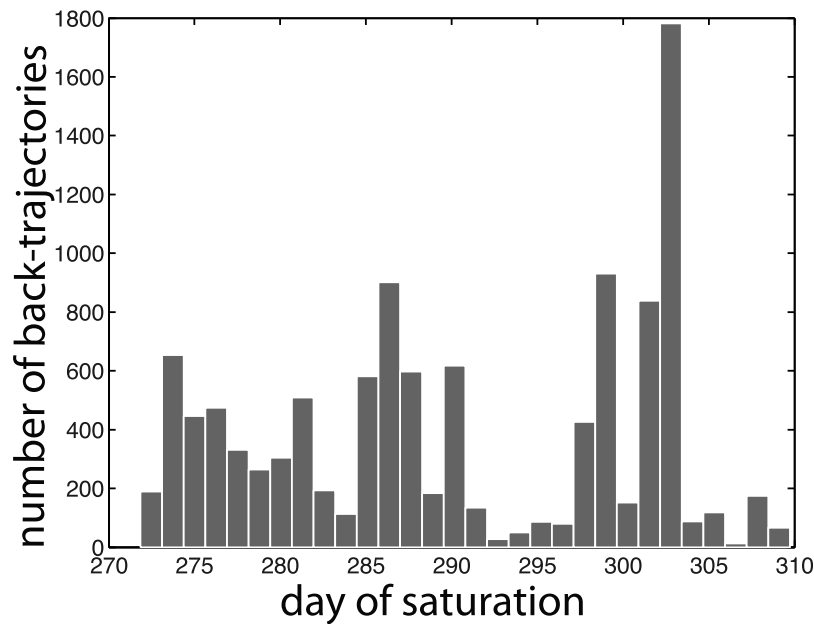


Figure 6. Histogram of the distribution of saturation events from the Lagrangian back-trajectory analysis, for all days between day 283 and day 311. Saturation events are concentrated around day 286 (12 October) and day 302 (28 October).

clouds explains the discrepancy. The improved Lagrangian reconstruction with a higher resolution wind field (ERA-Interim versus NCEP, Figure 10c) does indicate that errors in the wind field produce biases in the reconstructions.

[29] Time series of the isotope reconstructions are shown in Figures 10e and 10f. As was done for the reconstructions of q , in Figure 10f are both the NCEP and ERA-Interim reanalysis-based Lagrangian reconstructions for δD values. Time series curves for plus or minus one standard deviation are included for the ERA-Interim-based Lagrangian reconstruction (Figure 10f). The Lagrangian isotope reconstruction overestimates the magnitude and frequency of variability. The Eulerian (NCEP-based) reconstruction captures both the magnitude and frequency of the variability of the overnight δD values observed at the MLO. The correlation coefficients between the overnight observed water vapor δD values and both the Eulerian and Lagrangian-based reconstructions are $r = 0.63$ and $r = 0.47$. For comparison, the correlation between the IsoGSM output and the observations is $r = 0.24$. The means of the observed, and both the Eulerian and Lagrangian-based reconstructions are about; -249% , -242% , and -234% . Both models appear to capture the first order details of the observations (i.e., the mean, the range, and the 2 to 7 day variability). The Lagrangian reconstruction has larger differences on shorter time-scales and appears to overestimate the variability. The Eulerian MATCH time series (Figures 10b and 10e) appears smoother, compared with the Lagrangian time series (Figures 10c and 10f) because for the Eulerian approach, the LSPs are averaged across tracer domains effectively smoothing the data. The Lagrangian reconstructions, for both q and δD , based on the newer and higher resolution ERA-Interim Reanalysis are notably improved over the NCEP-based reconstructions meaning that by lessening the error in the reanalysis wind fields, the bias between observed and reconstructed values is reduced.

[30] The probability distributions of the Eulerian and Lagrangian reconstructions are both plotted in the q versus δD domain in Figure 11. For comparison, the distribution of observed overnight values are also shown, as are a pair of Rayleigh fractionation curves. Also shown in Figure 11 is the joint distribution of NCEP q versus IsoGSM δD values (Figure 11a). IsoGSM overestimates the observed δD values, which is motivation for better understanding the processes that influence subtropical water vapor isotope ratios in the subtropical free troposphere. The Rayleigh curves were constructed assuming an initial marine boundary layer vapor, with $\delta D = -90\%$. Here, the initial q value for the Rayleigh curves is dependent on the latitude-dependent q^* at the temperature of the LCL. For instance, the curves at the left originate at the q^* for saturation at a LCL temperature of 273°K and the curves at the right originate at the q^* for a LCL temperature of 298.5°K . The initial q^* at LCL for each Rayleigh curve is calculated from the Pacific-zonal and time-mean (for the measurement period) temperature from the Reanalysis. Because q^* at the LCL varies as a function latitude, distinct Rayleigh curves were calculated for each ten degree of latitude across the Pacific. The two curves in Figure 11 effectively represent Rayleigh fractionation, up from the LCL to last saturation, in both the extra-tropical storm-track region (50°N to 60°N) and near-Hawaii (10°N to 20°N). Most of the observed and reconstructed distributions are constrained by these Rayleigh curves [Noone *et al.*, 2011]. However, observed distributions during the most humid period (days 300 to 305) lie below even the warmer (right) Rayleigh curve. These observed isotope ratios for these moist-period data may reflect the amount-effect and enhanced fractionation associated with intense rainfall near Hawaii. The δD values of heavy rainfall at tropical latitudes are inversely related to the amount of precipitation [Dansgaard, 1964; Risi *et al.*, 2008]. Neither the Lagrangian

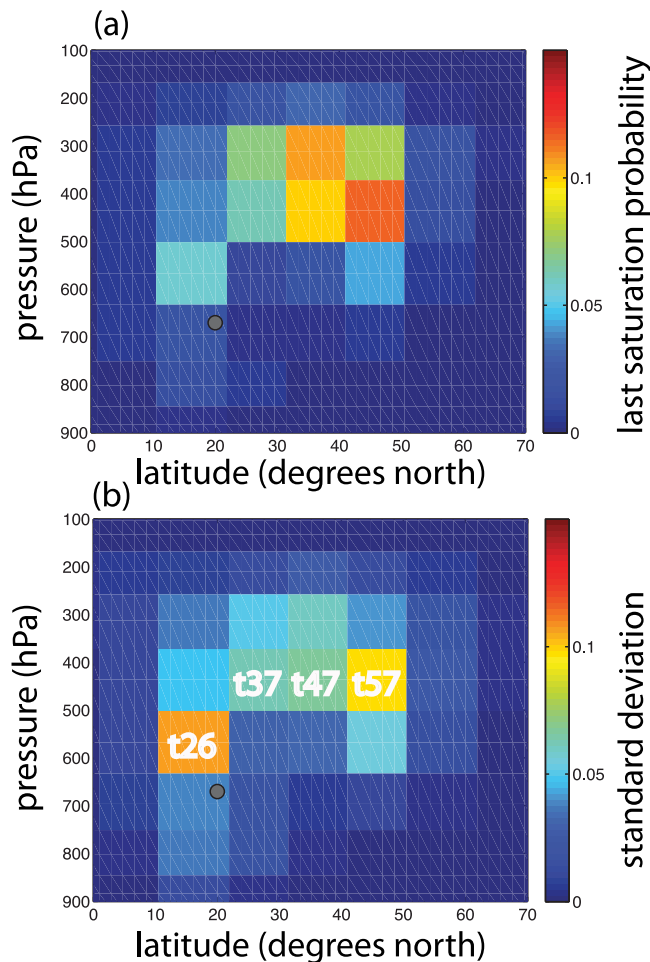


Figure 7. (a) Eulerian time-mean probability of last saturation. (b) Standard deviation of the probability of last saturation time series, using NCEP reanalysis. Position of MLO is shown by filled circles. Time series of last saturation probability are shown in Figure 8 for the four tracer domains (t26, t37, t47, and t57) labeled in Figure 7b.

nor the Eulerian reconstruction captures this detail of the observations. This is not surprising given that the Reanalyses do not resolve the observed higher humidity values. Additionally, neither reconstruction accounts for cloud physics or localized detrainment, which are essential to resolve the mechanisms affecting the water vapor isotope composition [Bony *et al.*, 2008; Lee and Fung, 2008; Moyer *et al.*, 1996; Risi *et al.*, 2008; Sayres *et al.*, 2010; Worden *et al.*, 2007], and which are limitations that bias them toward a result that is representative of the large-scale circulation.

[31] Figure 11 shows filled star symbols to represent the most likely distribution of observed q and δD values, and square symbols for the reconstructed values. The most commonly observed values of q and δD are centered about 2.6 g/kg and -268% . The most frequent of the Eulerian reconstructed values is centered at about 1.2 g/kg and -284% , and the most frequent value of the back-trajectory-based reconstructed values is centered at about 2.9 g/kg and -251% . The Eulerian reconstruction underestimates both q and δD , while the Lagrangian reconstruction overestimates

both q and δD . For higher humidity values ($q > 2$ g/kg), the Lagrangian reconstruction more closely approximates the observed q versus δD distributions. For low humidity values ($q \sim 1\text{--}2$ g/kg), the observed range of δD values is from -350% to less than -200% , and this range is better approximated by the Eulerian reconstruction. On the other hand, Lagrangian reconstructed δD values range from about -310% to -280% when q is less than 2 g/kg. The wide range of observed δD values for $q \sim 1.5$ g/kg demonstrates the usefulness of water vapor stable isotope ratios from the subtropical free troposphere. Similarly, for $\delta D \sim -200\%$, the observed range of q , though not continuous, is about an order of magnitude (1 to 10 g/kg). This sort of data distribution can be explained by a two-component mixing model, whereby a mixing line connects two points from opposite ends of a Rayleigh curve. This technique has been used to explain satellite observations [Noone, 2012], the MLO observations discussed here [Noone *et al.*, 2011], and tested in modeling studies, such as Galewsky and Hurley [2010]. Here, we consider the role of mixing in conjunction with last saturation along Rayleigh curves to reconcile the reconstructed time series with the observed distribution of q and δD values.

3.5. Role of Mixing

[32] To explore the role of mixing, we experiment with our last saturation model results. To reconcile results from the two approaches we degrade the Eulerian reconstructions to remove the role of mixing, and enhance the Lagrangian model by adding a small external moisture sources. To be clear, in the Eulerian mixing experiment, we reconstruct q and δD values assuming all of the air at MLO is from the tracer domain associated with the maximum LSP, to show the influence of air mass mixing within the free troposphere. In the Lagrangian mixing experiment, we test the sensitivity

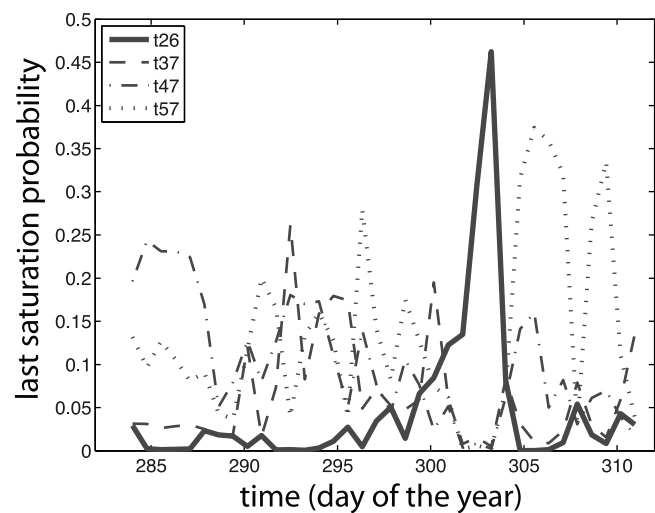


Figure 8. Time series of Eulerian last saturation probability for air at MLO. Solid line - near-Hawaiian tracer domain (t26); gray dashed, dotted, dash-dotted lines are for tracer domains in the extra-tropical upper troposphere (t37, t47, and t57). Tracer domain locations are shown in Figure 6.

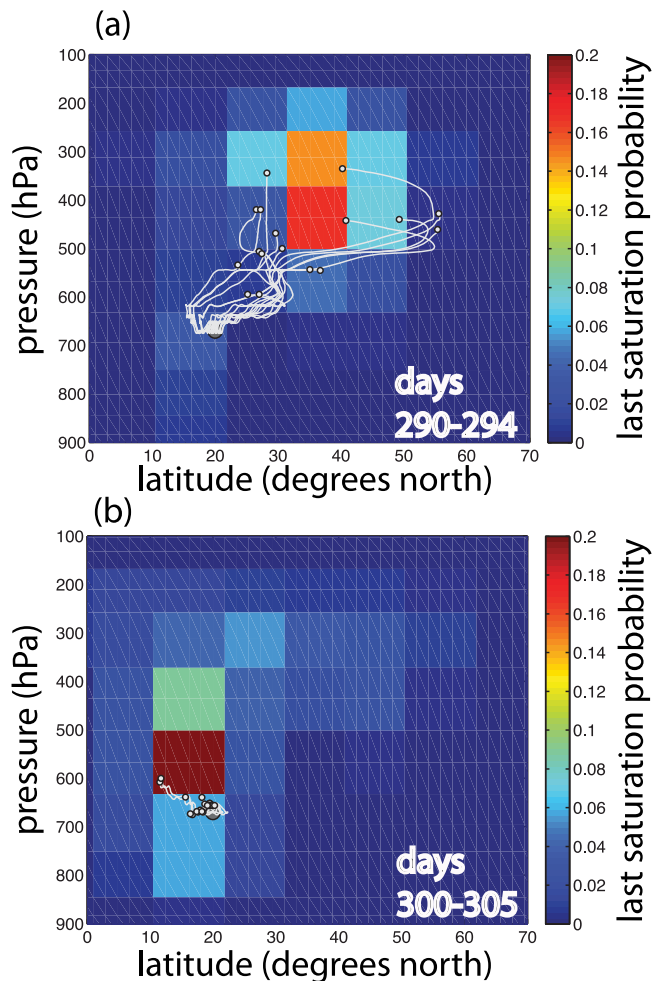


Figure 9. Time-mean of Eulerian last saturation probabilities for periods (a) from days 290 to 294, and (b) days 300 to 305, using NCEP reanalysis. Reference air at MLO indicated by white star. Lagrangian back-trajectories (solid white lines, using ERA-Interim reanalysis) terminate at last saturation (black circles).

of the Lagrangian results to variable amounts of mixing or influx of vapor from the marine boundary layer.

[33] In the first experiment, we assume that the water vapor at MLO comes solely from the tracer domain associated with the maximum LSP in an attempt to reduce the influence of mixing. Here we effectively set $q_{MLO}(t)$ and $\delta D_{MLO}(t)$ equal to q^* and δD at last saturation, from the tracer domain with the maximum LSP per time step. By doing so, we qualitatively assess the role of air mass mixing in setting subtropical humidity and stable isotope ratios. The result of this experiment (Figure 12) underestimates the observed q by less than half and underestimates observed δD values by about 100%. The temporal pattern for q matches the observations (Figure 12a) and the correlation coefficient between reconstructed and observed q is only slightly reduced, from 0.60 to 0.55. However, the tracer domain associated with the maximum LSP is typically at a high altitude and latitude position and so does not yield as much

water vapor as is observed at MLO. In contrast, the correlation coefficient between the reconstructed and observed δD values drops from 0.63 to 0.36 when we consider only the tracer domain associated with the maximum LSP. δD is more difficult, than humidity, to simulate without air mass mixing from various last saturation regions, which provides a reminder that isotope ratio information principally responds to differences in air mass history. Subtropical water vapor δD is not solely a function of local temperature, can vary independently of the local water vapor mixing ratio, and depends on the distribution of different processes setting the upstream isotopic composition. These include variations in air mass transport, mixing, and cloud microphysical controls.

[34] In the second experiment, we assess the role of mixing, from influx of vapor evaporated from the surface, by varying the mixing parameter (k) in the Lagrangian reconstructions and evaluate the resultant joint distribution of q and δD values. Best fit curves are plotted in Figure 13 that summarize q versus δD distributions for variable amounts of mixing k . The form of the Lagrangian solution for q is summarized by

$$q_{MLO} = (1 - k) \times [q^*_{lts}] + k \times [q_{lsrc}], \quad (5)$$

where q^*_{lts} is the q^* at Lagrangian last saturation along the back-trajectory, q_{lsrc} (20 g/kg) is the Lagrangian specific humidity from the marine boundary layer, and k is the mixing parameter. For δD , we follow equation (2), and vary the value of k . The original Lagrangian reconstructions presented in Figures 10 and 11 use k of 2 percent per hour ($k = 0.02$), whereas in Figure 13, we vary k from 0 to 8 percent per hour. This figure qualitatively depicts the role of mixing from the source water, where the curve for $k = 0$ approximates a Rayleigh curve and does not resemble the observations. This distribution is not exactly a single Rayleigh curve because it is a representation of mixing of air that was last saturated along a variety of Rayleigh curves. Inclusion of mixing of source water within the Lagrangian advection-condensation scheme allows us to more closely match the observations. Variable degrees of mixing can account for most of the observed range of q and δD distributions, except for the most humid observations, where δD observations are below the Rayleigh curves. As discussed earlier, these most humid observations could reflect moistening from mid-level clouds by processes that are not well represented by GCMs, and the hydrology of MATCH. From Figure 13, low q and δD values are best approximated with nonzero mixing. This prompted the use of the 2% mixing scenario for the reconstructions presented in Figures 10 and 11. This confirms that the advection-condensation approach, which posits that dry air masses are isolated from one another, while imperfect requires only a 2% per hour mixing of source vapor as a function of time since last saturation to describe the humidity. The isotopic information shows that mixing must be included to adequately capture the water mass hydrological balance.

4. Discussion and Conclusions

[35] On time scales of 2–7 days, nighttime δD values on Mauna Loa vary from about -300% to -200% and mixing ratios vary from less than about 1 to about 10 g/kg.

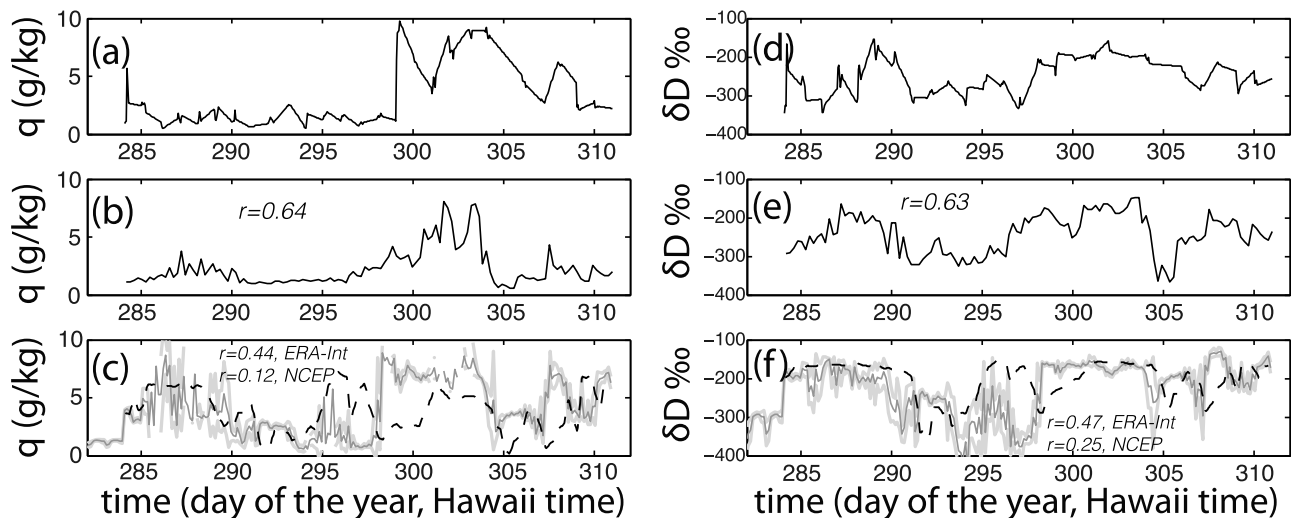


Figure 10. MLO specific humidity; (a) observed overnight and reconstructed from (b) Eulerian and (c) Lagrangian (ERA-Interim -solid; NCEP -dashed) last saturation models. MLO water vapor δD values; (d) observed overnight and reconstructed from (e) Eulerian and (f) Lagrangian (ERA-Interim -solid; NCEP -dashed) last saturation models. Correlation coefficients (r) are indicated for the reconstructed time series versus the observed overnight data. In Figures 10c and 10f are the curves for the plus or minus one standard deviation of the ERA-Interim-based Lagrangian reconstructions, as light gray solid lines.

Periods of low humidity and δD values at MLO correspond to enhanced LSP in midlatitude storms of the extra-tropical upper troposphere. Whereas, periods of higher humidity and δD values at MLO correspond to elevated LSP near Hawaii associated with mesoscale convection. This result agrees with recent field campaigns [Strong *et al.*, 2007] that demonstrate the relationship between vapor source and the time-varying isotope composition. Discrepancies between observed and reconstructed values for q and δD reflect the inability to fully reconcile gridded model output with point observations. Additionally, differences between observed and reconstructed values include limitations of the advection-condensation paradigm to correctly account for moistening processes, such as by cloud processes [Sherwood, 1999; Sherwood *et al.*, 2010] and mixing between otherwise isolated air masses [Noone *et al.*, 2011]. The results here highlight the role of mixing in setting the water vapor stable isotope ratio of dry subtropical air and furthermore provide insight to the role of mixing in a way that is typically neglected in traditional advection-condensation models. Although the implementation of a more sophisticated Lagrangian approach could account for errors and bias in parcel dispersion and track uncertainty [Emanuel and Pierrehumbert, 1996] in ways that the model used here does not, the result that mixing is required to reconcile the Lagrangian view with the Eulerian model and with observations is likely robust. From the experimental mixing reconstructions (Figures 12 and 13), we have shown that an advection-condensation scheme, together with a simple Rayleigh model, does not match the observed joint distribution of q and δD values. However, when mixing is included, both air mass mixing within the free troposphere and influx mixing of evaporated vapor from the source water, then the bias between observed and simulated values is reduced. This mixing is highly parameterized and intended only to indicate

that mixing can play an important role. Lessening of errors in the Reanalysis wind fields could also reduce the biases found at Mauna Loa. This is suggested by the improved reconstruction based on the more recent ERA-Interim Reanalysis compared with the NCEP based reconstruction (Figures 10c and 10f).

[36] Findings and conclusions are limited here by the one-month duration of our study. Having conducted the experiment in boreal autumn, we might have expected last saturation to be associated with midlatitude baroclinic activity because the storm track is most active in the cold season. It is not obvious what an LSP distribution might be for air at MLO during the boreal warm season. Suppression of midlatitude baroclinic activity during those months may yield enhanced LSP near-Hawaii and water vapor with high δD values at MLO. Also, it is not difficult to imagine that the seasonal cycle and inter-annual variability [Hurley and Galewsky, 2010a] of the water vapor isotope composition of the subtropical middle troposphere is linked to variability of mixing and the large-scale circulation. The role of mixing and advection-condensation in resolving longer period variability of subtropical water vapor isotope ratios remains unresolved and left for future research.

[37] Circulation and temperature changes associated with global warming are expected to alter the humidity of the subtropics, a critical aspect of the water vapor feedback [Galewsky and Hurley, 2010]. Given the projected humidity and circulation changes in response to global warming [Lorenz and DeWeaver, 2007; Lu *et al.*, 2007; Vecchi *et al.*, 2008; Yin, 2005] and the projected changes in LSP distributions [Hurley and Galewsky, 2010b; Wright *et al.*, 2010], we would expect the heavy to light stable isotope ratio of water vapor in the dry subtropics to be altered in ways that can be predicted by GCMs. Representation of these processes in GCMs can be

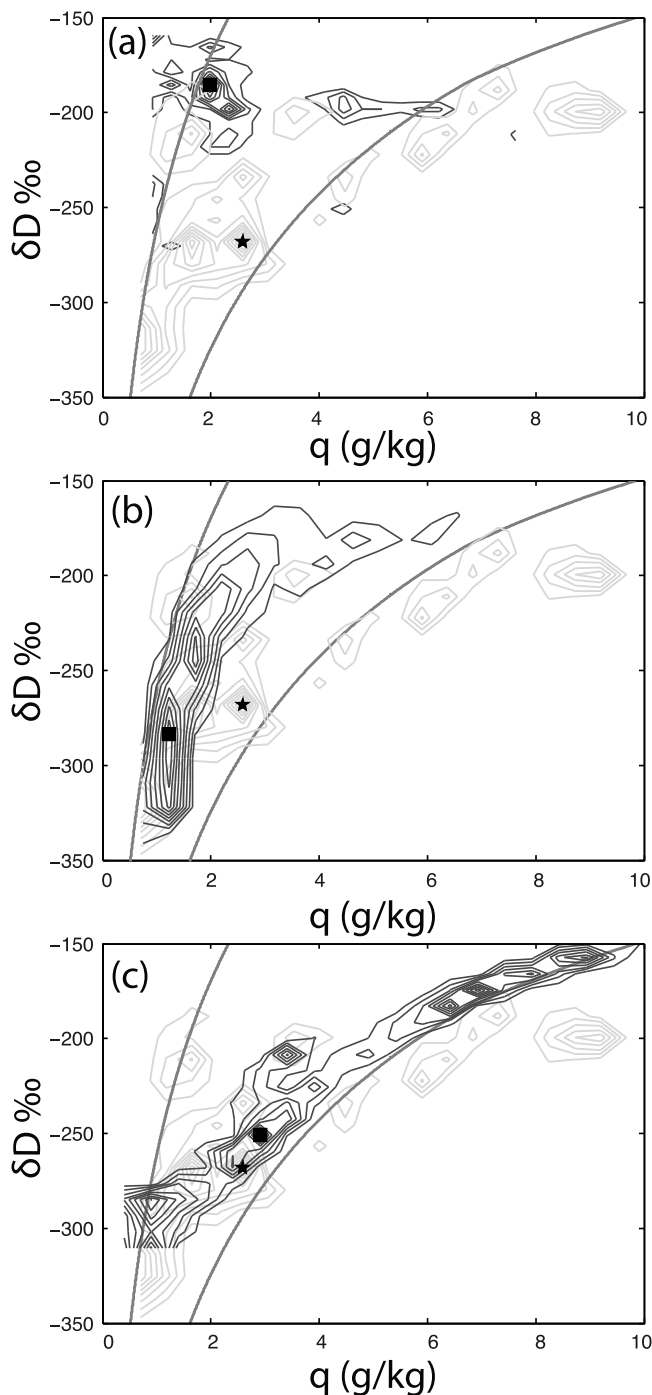


Figure 11. Joint normalized probability distributions of q and δD . (a) The observed overnight (gray contours) and the NCEP q with the IsoGSM δD values. (b and c) The observed overnight (gray contours) and the reconstructed (black contours) distributions. Contour intervals are 10%. Eulerian reconstructed values are plotted in Figure 11b and Lagrangian (ERA-Interim) reconstructed values are plotted in Figure 11c, both as black contours. Symbols (discussed in text) indicate maximum probability for reconstructions (squares) and observed overnight (stars). Rayleigh curve at left (right) begins at saturation specific humidity for lifting condensation level temperature of 273 K (298.5 K).

evaluated by comparing GCM output against observed q and δD values. δD provides an additional constraint on humidity, allowing assessment of GCM simulations of future humidity changes.

[38] This study is limited in that it does not account for moistening that may occur within the free troposphere (unrelated to the source water) following last saturation and we use a simple Rayleigh model that does not account for kinetic effects. Yet this simple approach can be used to account for much of the temporal variability of isotopes in the subtropical free troposphere. Finally, from this four-week period we find that about 1–3% per hour mixing of source vapor as a function of time since last saturation from the marine boundary layer improves our approximation of observed water vapor and isotope mixing ratios at MLO. Only a small fraction of mixing is required because the boundary layer has much greater humidity than the dry air

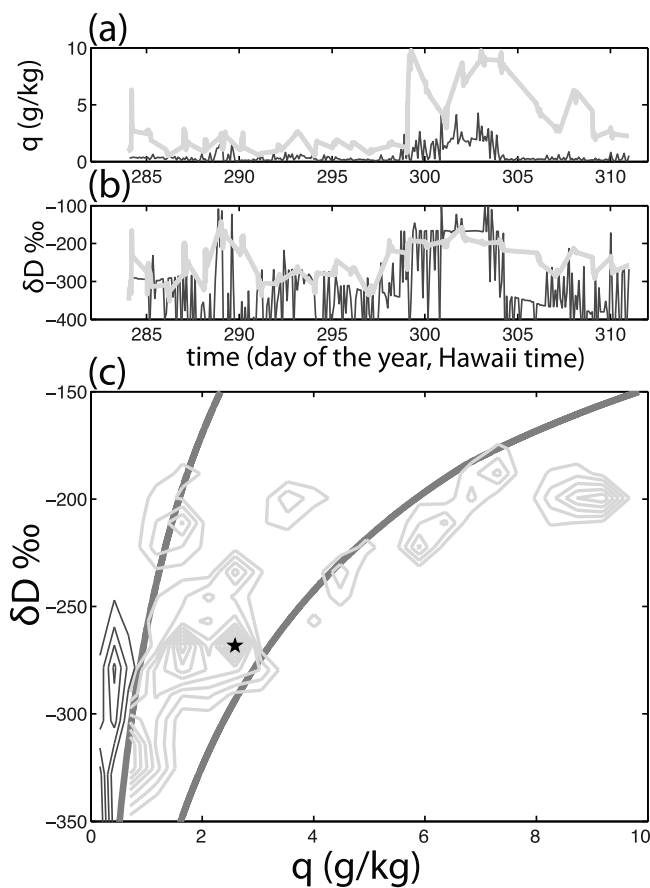


Figure 12. Eulerian mixing experiment. Time series of the Eulerian mixing experimental (solid black) and observed overnight (solid gray) (a) q (g/kg) and (b) δD (‰). (c) Joint normalized probability distributions of q and δD ; observed over-night (gray contours) and experimental reconstructed values (black contours). Contour intervals are 10%. Eulerian experimental reconstructed values (black contours) reflect a reconstruction assuming all of the air at MLO is from the tracer domain associated with the maximum probability. Star and Rayleigh curves are as in Figure 11. Maximum probability associated with the reconstructed values is off of the y axis to the bottom left.

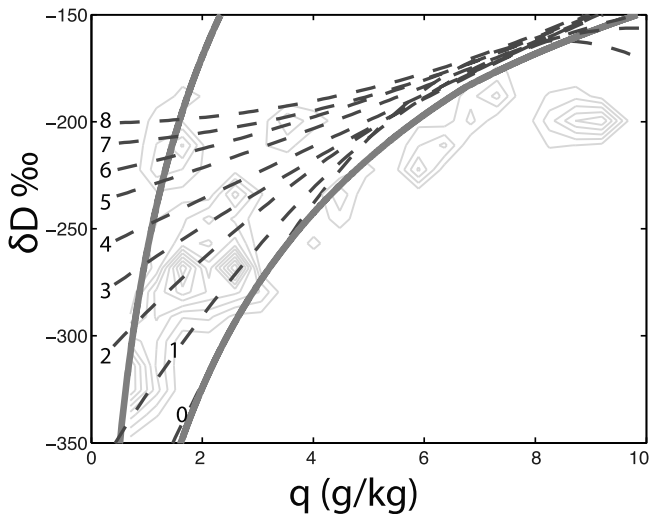


Figure 13. Lagrangian mixing experiment. Joint normalized probability distributions of q and δD ; observed overnight (gray contours) and experimental reconstructed best-fit curves (dashed lines). Contour intervals for the observations are 10%. Dashed lines are best-fit curves to the Lagrangian experimental reconstructed distributions for various degrees of mixing (0 to 8 percent).

saturated upstream. This finding suggests that even very infrequent exchange of moisture between the boundary layer and free troposphere can dramatically influence the moisture balance of the subtropics.

[39] **Acknowledgments.** We thank Editor Yinon Rudich and three anonymous reviewers for persistently helpful comments. We also thank Zachary D. Sharp, David Gutzler, Peter Fawcett, and Ken Minschwaner for thoughtful comments on an earlier version of the manuscript. NSF grant ATM-0840-168 supported J. Galewsky and NSF grant ATM-0840-129 supported D. Noone for this research. Part of this research was carried out at the Jet Propulsion Laboratory, California Institute of Technology, under a contract with the National Aeronautics and Space Administration. The NASA ROSES Aura Science Team NNH07ZDA001N-AST 07-AST07-0069 contributed to the support of the analysis.

References

- Berkelhammer, M., C. Risi, N. Kurita, and D. C. Noone (2012), The moisture source sequence for the Madden-Julian Oscillation as derived from satellite retrievals of HDO and H₂O, *J. Geophys. Res.*, *117*, D03106, doi:10.1029/2011JD016803.
- Bony, S., C. Risi, and F. Vimeux (2008), Influence of convective processes on the isotopic composition ($\delta^{18}\text{O}$ and δD) of precipitation and water vapor in the tropics: 1. Radiative-convective equilibrium and Tropical Ocean–Global Atmosphere–Coupled Ocean–atmosphere Response Experiment (TOGA-COARE) simulations, *J. Geophys. Res.*, *113*, D19305, doi:10.1029/2008JD009942.
- Brill, K., and B. Albrecht (1982), Diurnal variation of the trade-wind boundary layer, *Mon. Weather Rev.*, *110*(6), 601–613, doi:10.1175/1520-0493(1982)110<0601:DVOTTW>2.0.CO;2.
- Brown, D., J. Worden, and D. Noone (2008), Comparison of atmospheric hydrology over convective continental regions using water vapor isotope measurements from space, *J. Geophys. Res.*, *113*, D15124, doi:10.1029/2007JD009676.
- Cao, G. X., T. W. Giambelluca, D. E. Stevens, and T. A. Schroeder (2007), Inversion variability in the Hawaiian trade wind regime, *J. Clim.*, *20*(7), 1145–1160, doi:10.1175/JCLI4033.1.
- Cau, P., J. Methven, and B. Hoskins (2007), Origins of dry air in the tropics and subtropics, *J. Clim.*, *20*, 2745–2759, doi:10.1175/JCLI4176.1.
- Chepfer, H., S. Bony, D. Winker, M. Chiriaco, J. L. Dufresne, and G. Seze (2008), Use of CALIPSO lidar observations to evaluate the cloudiness

- simulated by a climate model, *Geophys. Res. Lett.*, *35*, L15704, doi:10.1029/2008GL034207.
- Cuffey, K. M., and F. Vimeux (2001), Covariation of carbon dioxide and temperature from the Vostok ice core after deuterium-excess correction, *Nature*, *412*(6846), 523–527, doi:10.1038/35087544.
- Dansgaard, W. (1964), Stable isotopes in precipitation, *Tellus*, *16*(4), 436–468, doi:10.1111/j.2153-3490.1964.tb00181.x.
- Dee, D. P., et al. (2011), The ERA-Interim reanalysis: Configuration and performance of the data assimilation system, *Q. J. R. Meteorol. Soc.*, *137*(656), 553–597, doi:10.1002/qj.828.
- Dessler, A. E., and S. M. Davis (2010), Trends in tropospheric humidity from reanalysis systems, *J. Geophys. Res.*, *115*, D19127, doi:10.1029/2010JD014192.
- Dessler, A. E., and K. Minschwaner (2007), An analysis of the regulation of tropical tropospheric water vapor, *J. Geophys. Res.*, *112*, D10120, doi:10.1029/2006JD007683.
- Draxler, R. R., and G. D. Hess (1997), Description of the HYSPLIT 4 modeling system, *NOAA Tech. Memo. ERL ARL-224*, 24 pp., NOAA Air Resour. Lab., Silver Spring, Md.
- Emanuel, K., and R. T. Pierrehumbert (Eds.) (1996), *Microphysical and Dynamical Control of Tropospheric Water Vapor*, 260 pp., Springer, Berlin.
- Galewsky, J., and J. V. Hurley (2010), An advection-condensation model for subtropical water vapor isotopic ratios, *J. Geophys. Res.*, *115*, D16116, doi:10.1029/2009JD013651.
- Galewsky, J., A. H. Sobel, and I. H. Held (2005), Diagnosing subtropical humidity dynamics using tracers of last saturation, *J. Atmos. Sci.*, *62*, 3353–3367, doi:10.1175/JAS3533.1.
- Galewsky, J., M. Strong, and Z. D. Sharp (2007), Measurements of water vapor D/H ratios from Mauna Kea, Hawaii, and implications for subtropical humidity dynamics, *Geophys. Res. Lett.*, *34*, L22808, doi:10.1029/2007GL031330.
- Gat, J. R. (1996), Oxygen and hydrogen isotopes in the hydrologic cycle, *Annu. Rev. Earth Planet. Sci.*, *24*, 225–262, doi:10.1146/annurev.earth.24.1.225.
- Gupta, P., D. Noone, J. Galewsky, C. Sweeney, and B. H. Vaughn (2009), Demonstration of high-precision continuous measurements of water vapor isotopologues in laboratory and remote field deployments using wavelength-scanned cavity ring-down spectroscopy (WS-CRDS) technology, *Rapid Commun. Mass Spectrom.*, *23*(16), 2534–2542, doi:10.1002/rcm.4100.
- Hansen, J., et al. (2005), Earth's energy imbalance: Confirmation and implications, *Science*, *308*(5727), 1431–1435, doi:10.1126/science.1110252.
- Held, I. M., and B. J. Soden (2000), Water vapor feedback and global warming, *Annu. Rev. Energy Environ.*, *25*, 441–475, doi:10.1146/annurev.energy.25.1.441.
- Hurley, J. V., and J. Galewsky (2010a), A last saturation analysis of ENSO humidity variability in the subtropical Pacific, *J. Clim.*, *23*(4), 918–931, doi:10.1175/2009JCLI193.1.
- Hurley, J. V., and J. Galewsky (2010b), A last-saturation diagnosis of subtropical water vapor response to global warming, *Geophys. Res. Lett.*, *37*, L06702, doi:10.1029/2009GL042316.
- Iannone, R. Q., D. Romanini, O. Cattani, H. A. J. Meijer, and E. R. T. Kerstel (2010), Water isotope ratio ($\delta^2\text{H}$ and $\delta^{18}\text{O}$) measurements in atmospheric moisture using an optical feedback cavity enhanced absorption laser spectrometer, *J. Geophys. Res.*, *115*, D10111, doi:10.1029/2009JD012895.
- Johnson, L. R., Z. D. Sharp, J. Galewsky, M. Strong, A. D. Van Pelt, F. Dong, and D. Noone (2011), Hydrogen isotope correction for laser instrument measurement bias at low water vapor concentration using conventional isotope analyses: Application to measurements from Mauna Loa Observatory, Hawaii, *Rapid Commun. Mass Spectrom.*, *25*(5), 608–615, doi:10.1002/rcm.4894.
- Jouzel, J., C. Lorius, J. R. Petit, C. Genthon, N. I. Barkov, V. M. Kotlyakov, and V. M. Petrov (1987), Vostok ice core—A continuous isotope temperature record over the last climatic cycle (160,000 years), *Nature*, *329*(6138), 403–408, doi:10.1038/329403a0.
- Kalnay, E., et al. (1996), The NCEP/NCAR 40-years reanalysis project, *Bull. Am. Meteorol. Soc.*, *77*, 437–471, doi:10.1175/1520-0477(1996)077<0437:TNYRP>2.0.CO;2.
- Lee, J. E., and I. Fung (2008), “Amount effect” of water isotopes and quantitative analysis of post-condensation processes, *Hydrol. Processes*, *22*(1), 1–8, doi:10.1002/hyp.6637.
- Lis, G., L. I. Wassenaar, and M. J. Hendry (2008), High-precision laser spectroscopy D/H and $^{18}\text{O}/^{16}\text{O}$ measurements of microliter natural water samples, *Anal. Chem.*, *80*(1), 287–293, doi:10.1021/ac701716q.
- Lorenz, D. J., and E. T. DeWeaver (2007), The response of the extratropical hydrological cycle to global warming, *J. Clim.*, *20*, 3470–3484, doi:10.1175/JCLI4192.1.

- Lu, J., G. A. Vecchi, and T. Reichler (2007), Expansion of the Hadley cell under global warming, *Geophys. Res. Lett.*, *34*, L06805, doi:10.1029/2006GL028443.
- Moyer, E. J., F. W. Irion, Y. L. Yung, and M. R. Gunson (1996), ATMOS stratospheric deuterated water and implications for troposphere-stratosphere transport, *Geophys. Res. Lett.*, *23*(17), 2385–2388, doi:10.1029/96GL01489.
- Noone, D. (2008), The influence of midlatitude and tropical overturning circulation on the isotopic composition of atmospheric water vapor and Antarctic precipitation, *J. Geophys. Res.*, *113*, D04102, doi:10.1029/2007JD008892.
- Noone, D. (2012), Pairing measurements of the water vapor isotope ratio with humidity to deduce atmospheric moistening and dehydration in the tropical mid-troposphere, *J. Clim.*, *25*, 4476–4494, doi:10.1175/JCLI-D-11-00582.1.
- Noone, D., et al. (2011), Properties of air mass mixing and humidity in the subtropics from measurements of the D/H isotope ratio of water vapor at the Mauna Loa Observatory, *J. Geophys. Res.*, *116*, D22113, doi:10.1029/2011JD015773.
- Payne, V. H., D. Noone, A. Dudhia, C. Piccolo, and R. G. Grainger (2007), Global satellite measurements of HDO and implications for understanding the transport of water vapour into the stratosphere, *Q. J. R. Meteorol. Soc.*, *133*(627), 1459–1471, doi:10.1002/qj.127.
- Pfahl, S., and H. Wernli (2008), Air parcel trajectory analysis of stable isotopes in water vapor in the eastern Mediterranean, *J. Geophys. Res.*, *113*, D20104, doi:10.1029/2008JD009839.
- Pierrehumbert, R. T., and R. Roca (1998), Evidence for control of Atlantic subtropical humidity by large scale advection, *Geophys. Res. Lett.*, *25*(24), 4537–4540, doi:10.1029/1998GL900203.
- Pierrehumbert, R. T., H. Brogniez, and R. Roca (2007), On the relative humidity of the atmosphere, in *The Global Circulation of the Atmosphere*, edited by T. Schneider and A. Sobel, pp. 143–185, Princeton Univ. Press, Princeton, N. J.
- Rasch, P. J., N. M. Mahowald, and B. E. Eaton (1997), Representations of transport, convection, and the hydrologic cycle in chemical transport models: Implications for the modeling of short-lived and soluble species, *J. Geophys. Res.*, *102*(D23), 28,127–28,138, doi:10.1029/97JD02087.
- Risi, C., S. Bony, and F. Vimeux (2008), Influence of convective processes on the isotopic composition ($\delta^{18}\text{O}$ and δD) of precipitation and water vapor in the tropics: 2. Physical interpretation of the amount effect, *J. Geophys. Res.*, *113*, D19306, doi:10.1029/2008JD009943.
- Risi, C., S. Bony, F. Vimeux, and J. Jouzel (2010), Water-stable isotopes in the LMDZ4 general circulation model: Model evaluation for present-day and past climates and applications to climatic interpretations of tropical isotopic records, *J. Geophys. Res.*, *115*, D12118, doi:10.1029/2009JD013255.
- Risi, C., et al. (2012a), Process-evaluation of tropospheric humidity simulated by general circulation models using water vapor isotopic observations: 2. Using isotopic diagnostics to understand the mid and upper tropospheric moist bias in the tropics and subtropics, *J. Geophys. Res.*, *117*, D05304, doi:10.1029/2011JD016623.
- Risi, C., et al. (2012b), Process-evaluation of tropospheric humidity simulated by general circulation models using water vapor isotopologues: 1. Comparison between models and observations, *J. Geophys. Res.*, *117*, D05303, doi:10.1029/2011JD016621.
- Sayres, D. S., L. Pfister, T. F. Hanisco, E. J. Moyer, J. B. Smith, J. M. St Clair, A. S. O'Brien, M. F. Witinski, M. Legg, and J. G. Anderson (2010), Influence of convection on the water isotopic composition of the tropical tropopause layer and tropical stratosphere, *J. Geophys. Res.*, *115*, D00J20, doi:10.1029/2009JD013100.
- Sharp, Z. D. (2006), *Principles of Stable Isotope Geochemistry*, Pearson Prentice Hall, Upper Saddle River, N. J.
- Sherwood, S. C. (1996), Maintenance of the free-tropospheric tropical water vapor distribution. Part I: Clear regime budget, *J. Clim.*, *9*, 2903–2918, doi:10.1175/1520-0442(1996)009<2903:MOTFTT>2.0.CO;2.
- Sherwood, S. C. (1999), On moistening of the tropical troposphere by cirrus clouds, *J. Geophys. Res.*, *104*(D10), 11,949–11,960, doi:10.1029/1999JD900162.
- Sherwood, S. C., R. Roca, T. M. Weckwerth, and N. G. Andronova (2010), Tropospheric water vapor, convection, and climate, *Rev. Geophys.*, *48*, RG2001, doi:10.1029/2009RG000301.
- Simmons, A., S. Uppala, D. Dee, and S. Kobayashi (2007), ERA-Interim: New ECMWF reanalysis products from 1989 onwards, *ECMWF Newsl.*, *110*, 25–35.
- Strong, M., Z. D. Sharp, and D. S. Gutzler (2007), Diagnosing moisture transport using D/H ratios of water vapor, *Geophys. Res. Lett.*, *34*, L03404, doi:10.1029/2006GL028307.
- Sun, D. Z., and R. S. Lindzen (1993), Distribution of tropical tropospheric water vapor, *J. Atmos. Sci.*, *50*(12), 1643–1660, doi:10.1175/1520-0469(1993)050<1643:DOTTWV>2.0.CO;2.
- Tans, P., and K. Thoning (2008), About CO₂ measurements, report, ESRL, NOAA, Boulder, Colo.
- Vecchi, G. A., A. Clement, and B. J. Soden (2008), Examining the tropical Pacific's response to global warming, *Eos Trans. AGU*, *89*(9), 81, 83, doi:10.1029/2008EO090002.
- Woolnough, S. J., et al. (2010), Modelling convective processes during the suppressed phase of a Madden-Julian Oscillation: Comparing single-column models with cloud-resolving models, *Q. J. R. Meteorol. Soc.*, *136*(647), 333–353, doi:10.1002/qj.568.
- Worden, J., D. Noone, K. Bowman, and Tropospheric Emission Spectrometer Science Team and Data contributors (2007), Importance of rain evaporation and continental convection in the tropical water cycle, *Nature*, *445*(7127), 528–532, doi:10.1038/nature05508.
- Worden, J., D. Noone, J. Galewsky, A. Bailey, K. Bowman, D. Brown, J. V. Hurley, S. Kulawik, J. Lee, and M. Strong (2010), Estimate of bias in Aura HDO/H₂O profiles from comparison of TES and in situ HDO/H₂O measurements at the Mauna Loa Observatory, *Atmos. Chem. Phys.*, *10*(11), 25,355–25,388, doi:10.5194/acpd-10-25355-2010.
- Wright, J., A. H. Sobel, and G. A. Schmidt (2009), The influence of condensate evaporation on water vapor and its stable isotopes in a GCM, *Geophys. Res. Lett.*, *36*, L12804, doi:10.1029/2009GL038091.
- Wright, J., A. Sobel, and J. Galewsky (2010), Diagnosis of zonal mean relative humidity changes in a warmer climate, *J. Clim.*, *23*, 4556–4569, doi:10.1175/2010JCLI3488.1.
- Yin, J. H. (2005), A consistent poleward shift of the storm tracks in simulations of 21st century climate, *Geophys. Res. Lett.*, *32*, L18701, doi:10.1029/2005GL023684.
- Yoshimura, K., M. Kanamitsu, D. Noone, and T. Oki (2008), Historical isotope simulation using Reanalysis atmospheric data, *J. Geophys. Res.*, *113*, D19108, doi:10.1029/2008JD010074.
- Zhang, G. J., and N. A. McFarlane (1995), Sensitivity of climate simulations to the parameterization of cumulus convection in the Canadian Climate Center General-Circulation Model, *Atmos. Ocean*, *33*(3), 407–446, doi:10.1080/07055900.1995.9649539.
- Zhang, Y., S. A. Klein, J. Boyle, and G. G. Mace (2010), Evaluation of tropical cloud and precipitation statistics of Community Atmosphere Model version 3 using CloudSat and CALIPSO data, *J. Geophys. Res.*, *115*, D12205, doi:10.1029/2009JD012006.